

# Local structural distortions drive magnetic molecular field in compositionally complex spinel oxide

Rukma Nevgi,<sup>1,\*</sup> Subha Dey,<sup>1,†</sup> Nandana Bhattacharya,<sup>1</sup> Soheil Ershadrad,<sup>2</sup>  
Tinku Dan,<sup>3</sup> Sujay Chakravarty,<sup>4</sup> S. D. Kaushik,<sup>5</sup> Christoph Klewe,<sup>6</sup>  
George E. Sterbinsky,<sup>7</sup> Biplab Sanyal,<sup>2</sup> and Srimanta Middey<sup>1,‡</sup>

<sup>1</sup>*Department of Physics, Indian Institute of Science, Bengaluru 560012, India*

<sup>2</sup>*Department of Physics and Astronomy,*

*Uppsala University, Box-516, 75120 Uppsala, Sweden*

<sup>3</sup>*Deutsches Elektronen-Synchrotron DESY, 22607 Hamburg, Germany*

<sup>4</sup>*UGC-DAE CSR Kalpakkam Node Kokilamedu-603104, Tamilnadu, India*

<sup>5</sup>*UGC-DAE Consortium for Scientific Research Mumbai Centre,  
R5 Shed, Bhabha Atomic Research Centre, Mumbai 400085, India*

<sup>6</sup>*Advanced Light Source, Lawrence Berkeley National  
Laboratory, Berkeley, California 94720, USA*

<sup>7</sup>*Advanced Photon Source, Argonne National Laboratory, Lemont, Illinois 60439, USA*

## Abstract

Understanding how local distortions determine the functional properties of high entropy materials, containing five or more elements at a crystallographic site, is an open challenge. We address this for a compositionally complex spinel oxide  $(\text{Mn}_{0.2}\text{Co}_{0.2}\text{Ni}_{0.2}\text{Cu}_{0.2}\text{Zn}_{0.2})\text{Cr}_2\text{O}_4$  ( $A^5\text{Cr}_2\text{O}_4$ ). By comparatively examining extended X-ray absorption fine structure on  $A^5\text{Cr}_2\text{O}_4$  and its parent counterparts  $A\text{Cr}_2\text{O}_4$  along with density functional theory calculations for multiple configurations, we find that the element-specific distortions go beyond the first neighbor. Specifically, the strong Jahn-Teller distortion present in  $\text{CuCr}_2\text{O}_4$  is found to be completely suppressed in  $A^5\text{Cr}_2\text{O}_4$ . Instead, there is a broad distribution of Cu-O and Cu-Cr bond distances while other A-O distances acquire certain specific values. This study demonstrates the additional flexibility of a cationic sublattice in maintaining a uniform long-range structure, in contrast to previous reports showing only the accommodative anionic sublattice. Remarkably, despite the presence of multiple magnetic ions and variable bond lengths, the mean field magnetic interactions of  $A^5\text{Cr}_2\text{O}_4$  exhibit a striking resemblance to those of  $\text{NiCr}_2\text{O}_4$ . This compelling observation originates from the comparability of bond lengths around Cr in both materials. Our study paves the way for a deeper understanding of the impact of local structural distortions in compositionally complex quantum materials, enabling the targeted design with tailored properties.

The periodic arrangement of atoms/ions/molecules within crystalline materials is the backbone of their diverse electronic, magnetic, and topological properties. Conventionally, crystalline materials are synthesized based on the principle of enthalpy minimization. However, in recent years, there has been a surge of interest in high-entropy materials that break this paradigm, where high configurational entropy drives structure formation [1–7]. Originally introduced for multicomponent alloys [8, 9], this concept was extended to oxide ceramics in 2015 by demonstrating the stabilization of  $\text{Mg}_{0.2}\text{Co}_{0.2}\text{Ni}_{0.2}\text{Cu}_{0.2}\text{Zn}_{0.2}\text{O}$  in a rock-salt structure [10]. Since then, high entropy oxides (HEOs) have been synthesized with a variety of structures, such as fluorites ( $\text{AO}_{2-\delta}$ ) [11], perovskites ( $\text{ABO}_3$ ) [12–15], spinels ( $\text{AB}_2\text{O}_4$ ) [16–18], and pyrochlores ( $\text{A}_2\text{B}_2\text{O}_7$ ) [19–21], where at least one of the crystallographic sites is occupied by five or more elements in equal or nearly equal atomic fractions. Despite not all being entropy-stabilized [5], these compositionally complex oxides (CCOs) exhibit interesting properties beyond their single element counterparts and hold potential for applications such as energy storage, catalysis, and microwave absorption, etc. [22–28].

Local lattice distortions [Fig. 1(a),(b)] in high entropy alloys (HEAs), a critical factor influencing their mechanical and physical properties, remain an open issue [29]. The presence of multiple sublattices adds further challenges in comprehending the interplay among disorder, distortions, and electronic/magnetic properties in CCO [30]. In conventional oxides with low disorder, distortions around individual cations are generally related to their ionic radii, coordination numbers, and oxidation states, which control electron hopping and magnetic exchange interaction strength. The local distortions around each cation within the disordered sublattice of CCO are expected to be highly variable and likely to deviate significantly from the average long-range structure probed by the diffraction technique. It is also necessary to determine the extent of this local distortion variation across neighboring elements and how it affects the material’s properties. To address these issues, we employ the extended X-ray absorption fine structure (EXAFS) technique, which is an element-specific method used to study the local chemical distribution (length scale  $\sim 1\text{-}10$  Å) around particular atoms [31–33]. EXAFS spectra are specifically sensitive to the coordination number, bond distances, and atomic species surrounding the core atom, providing a relatively simple way to understand the local structural distortion. Interestingly, EXAFS studies have shown that the variation in cation-specific bond lengths is confined only to the first coordination shell in the case of rock-salt HEOs [34, 35]. In this work, we examine the role of local distortions in modulating the magnetic characteristics of spinel oxide in a compositionally complex setting.

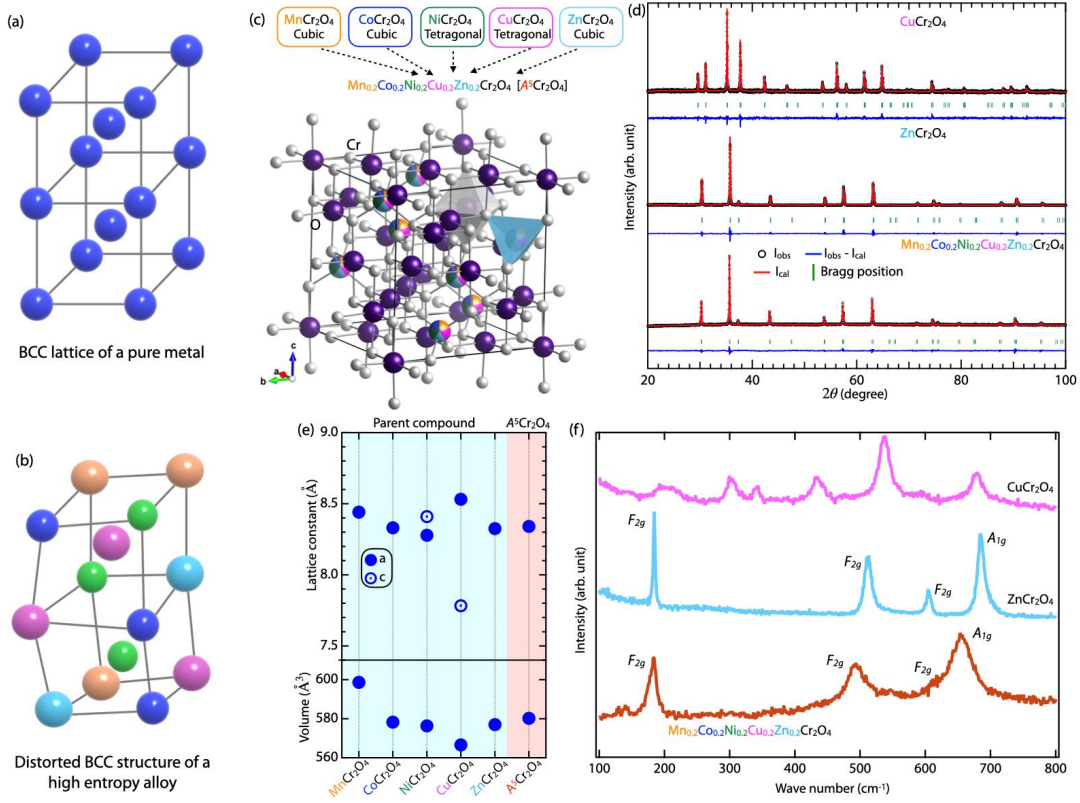


**FIG. 1. Long-range structural characterization.** Schematic to show (a) body centered cubic (BCC) lattice structure of a pure metal, and (b) a distorted BCC structure for a high entropy alloy with five five different elements present in near equal fraction. **c** Schematic of  $A^5Cr_2O_4$  with cubic spinel structure having Cr at the octahedral site and A (= Mn, Co, Ni, Cu and Zn) at the tetrahedral site. **d** Rietveld refined XRD data for  $CuCr_2O_4$  and  $ZnCr_2O_4$  along with  $A^5Cr_2O_4$ . **e** The lattice parameters for the parent compounds and  $A^5Cr_2O_4$  as obtained from the Rietveld analysis. The parameter  $a$  in the tetragonal phases of  $NiCr_2O_4$  and  $CuCr_2O_4$  have been multiplied by  $\sqrt{2}$  for ease of comparison. **f** Raman spectra of  $A^5Cr_2O_4$  has been compared with cubic  $ZnCr_2O_4$  and tetragonal  $CuCr_2O_4$ . The allowed Raman modes for cubic and tetragonal spinels are  $A_{1g}+E_g+3F_{2g}$ , and  $2A_{1g}+B_{1g}+3B_{2g}+4E_g$ , respectively [36, 37]. In our experiments, we found 4 modes for cubic and 8 modes for tetragonal compounds.

The normal  $AB_2O_4$  spinel consists of a diamond lattice formed by the tetrahedrally coordinated A site and a pyrochlore lattice formed by the octahedrally coordinated B site [Fig. 1(c)]. The spinel family has been extensively studied for over a century due to the observation of various phenomena, such as magnetic ordering, frustrated magnetism, orbital ordering, charge ordering,

metal-insulator transitions, etc [38]. We focused on the  $ACr_2O_4$  family of compounds with normal spinel structures and have synthesized  $(Mn_{0.2}Co_{0.2}Ni_{0.2}Cu_{0.2}Zn_{0.2})Cr_2O_4$  (hereafter referred to as  $A^5Cr_2O_4$ ). The individual members  $MnCr_2O_4$  and  $CoCr_2O_4$  are cubic and become ferrimagnetic at  $T_c$  values of 41 K and 93 K, respectively [39–42]. Additionally, they exhibit multiferroic behavior below 18 K and 27 K [39–42]. Due to the Jahn-Teller activity of the  $Ni^{2+}$  and  $Cu^{2+}$  ions,  $NiCr_2O_4$  and  $CuCr_2O_4$  undergo cubic to tetragonal transitions below 310 K and 853 K, respectively. They transform into an orthorhombic phase at 65 K and 125 K, respectively, accompanied by a ferrimagnetic transition [43]. On the other hand,  $ZnCr_2O_4$  is cubic at room temperature and exhibits an antiferromagnetic ordering transition below 12 K [44].

In the present work, we probe the modification of the local structure of  $A^5Cr_2O_4$  compared to that of its five undoped counterparts ( $ACr_2O_4$ ,  $A = Mn, Co, Ni, Cu, Zn$ ) at room temperature. X-ray diffraction (XRD), Raman spectroscopy, and X-ray absorption spectroscopy (XAS) of the transition metal  $L_{3,2}$  edges confirmed the desired normal spinel structure of  $A^5Cr_2O_4$  with cubic symmetry. Our comprehensive EXAFS measurements and density functional theory (DFT) based calculations revealed the element-specific local structural distortions in  $A^5Cr_2O_4$  persist beyond the first neighbor. Interestingly, the Jahn-Teller distortions typically observed in the  $CuCr_2O_4$  are absent in  $A^5Cr_2O_4$ . Rather,  $CuO_4$  units are highly flexible to accommodate local distortions while maintaining a uniform long-range cubic structure. Furthermore, we demonstrate that these Cr-O and Cr-Cr bond lengths directly control the mean-field magnetic interaction energies.

## Results:

**Synthesis and global structural symmetry:** The synthesis of polycrystalline samples of five parent compounds  $ACr_2O_4$  ( $A = Mn, Co, Ni, Cu$  and  $Zn$ ) and  $A^5Cr_2O_4$  was carried out using a conventional solid-state synthesis route (details are provided in the Methods section). The powder X-ray diffraction (XRD) pattern of  $A^5Cr_2O_4$  at room temperature is compared with that of two parent members, tetragonal  $CuCr_2O_4$  and cubic  $ZnCr_2O_4$ , in Fig. 1(d). Similar to  $ZnCr_2O_4$ , the diffraction pattern of  $A^5Cr_2O_4$  can be indexed and refined with a normal spinel structure with cubic symmetry having a space group of  $Fd\bar{3}m$  (space group number: 227). The diffraction patterns and structural information obtained from the refinement of all six compounds are shown in the Supplementary (Table S1 and Fig. S1). The lattice constants and lattice volumes of five parent members and  $A^5Cr_2O_4$  at room temperature are shown in Fig. 1(e). For comparison, the lattice constant  $a$  of the tetragonal members  $NiCr_2O_4$  and  $CuCr_2O_4$  is multiplied by  $\sqrt{2}$  (see Supplementary Fig. S2). The trend in lattice parameters and volume can be understood by considering the

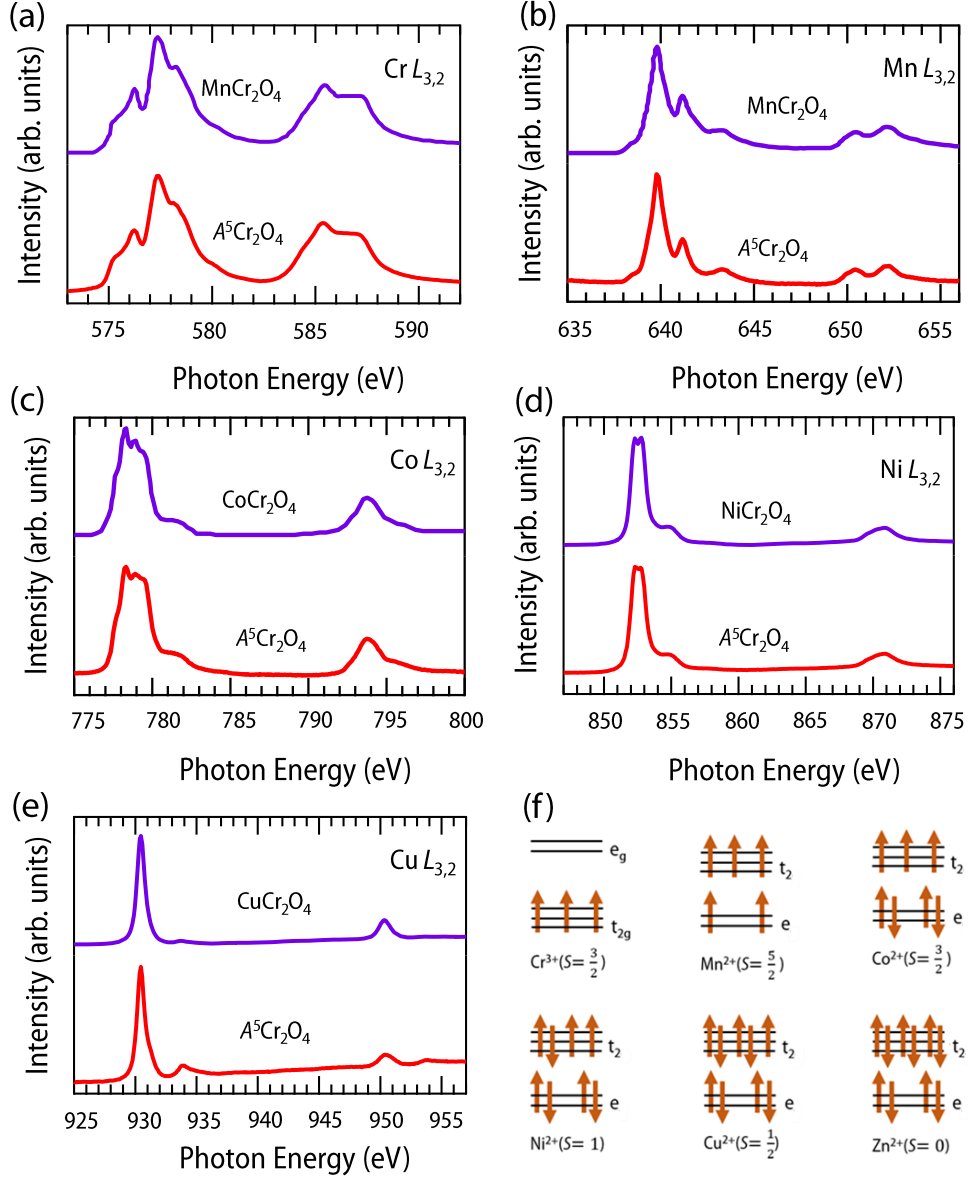


FIG. 2. **Determination of oxidation state using X-ray absorption spectroscopy.** **a** Cr  $L_{3,2}$  edge in  $MnCr_2O_4$  and  $A^5Cr_2O_4$ . **b** Mn  $L_{3,2}$  edge in  $MnCr_2O_4$  and  $A^5Cr_2O_4$ . **c** Co  $L_{3,2}$  edge in  $CoCr_2O_4$  and  $A^5Cr_2O_4$ . **d** Ni  $L_{3,2}$  edge in  $NiCr_2O_4$  and  $A^5Cr_2O_4$ . **e** Cu  $L_{3,2}$  edge in  $CuCr_2O_4$  and  $A^5Cr_2O_4$ . The spectra of Cr and Mn for  $MnCr_2O_4$  is taken from Ref. 45. The spectra of Co for  $CoCr_2O_4$  is adapted from Ref. 46. **f** Spin configurations of Cr, Mn, Co, Ni, Cu, and Zn cations in  $A^5Cr_2O_4$ . The energy gap between  $t_{2g}$  ( $t_2$ ) and  $e_g$  ( $e$ ) is not according to the scale.

ionic radii of  $A^{2+}$  ions. The average ionic radii (0.592 Å) of the  $A$ -site for  $A^5\text{Cr}_2\text{O}_4$  are closer to those of  $\text{Zn}^{2+}$  (0.60 Å) and  $\text{Co}^{2+}$  (0.58 Å) [ionic radii of  $\text{Mn}^{2+}$ : 0.66 Å,  $\text{Ni}^{2+}$ : 0.55 Å, and  $\text{Cu}^{2+}$ : 0.57 Å] [47], leading to similar unit cell volumes of  $A^5\text{Cr}_2\text{O}_4$  and  $A\text{Cr}_2\text{O}_4$  ( $A = \text{Co}$  and  $\text{Zn}$ ). Although  $\text{NiCr}_2\text{O}_4$  is tetragonal, the Jahn-Teller distortion is very small at 300 K, and the unit cell volume is very similar. It can also be inferred from Fig. 1(e) that the Mn and Cu ions are likely to experience internal stress (compressive for Mn and tensile for Cu) when introduced into  $A^5\text{Cr}_2\text{O}_4$ , leading to local structural distortions.

The Raman spectrum of  $A^5\text{Cr}_2\text{O}_4$  has been further compared with cubic  $\text{ZnCr}_2\text{O}_4$  and tetragonal  $\text{CuCr}_2\text{O}_4$  at Fig. 1(f).  $\text{ZnCr}_2\text{O}_4$  shows  $F_{2g}(1)$ ,  $F_{2g}(2)$ ,  $F_{2g}(3)$  and  $A_{1g}$  modes at  $185\text{ cm}^{-1}$ ,  $511\text{ cm}^{-1}$ ,  $604\text{ cm}^{-1}$ ,  $684\text{ cm}^{-1}$ , respectively, similar to earlier report [36]. Due to the lower symmetry,  $\text{CuCr}_2\text{O}_4$  exhibits additional Raman modes [37]. The similarity between the Raman spectra of  $A^5\text{Cr}_2\text{O}_4$  and  $\text{ZnCr}_2\text{O}_4$  further establishes its cubic symmetry. More significantly, we observe shifts and broadening of Raman modes, providing direct evidence of substantial lattice distortions within the compositionally complex  $A^5\text{Cr}_2\text{O}_4$  [48], which we probe further in detail using element-sensitive EXAFS technique.

**Transition metal valency and crystal field environment:** Prior to investigating local distortions, we determine the location of cations within octahedral and tetrahedral sites. For this, we carried out element-specific XAS experiments on the  $L_{3,2}$  edges of transition metal ions because the XAS spectral line shape for the  $2p^63d^n \rightarrow 2p^53d^{n+1}$  transition is strongly dependent on the valency, spin character of the initial state and crystal field environment of the system [49]. The XAS spectra for the  $L_{3,2}$  edges of Cr, Mn, Co, Ni, and Cu in  $A^5\text{Cr}_2\text{O}_4$ , recorded in total electron yield mode, were compared with those of the corresponding parent compounds, as shown in Fig. 2 (a)-(e). In all parent  $A\text{Cr}_2\text{O}_4$  compounds, the cations  $A^{2+}$  occupy the tetrahedral site, while  $\text{Cr}^{3+}$  occupies the octahedral site [38]. It is evident from Fig. 2 (a)-(e) that the spectra of Cr, Mn, Co, and Ni for  $A^5\text{Cr}_2\text{O}_4$  look exactly similar to the corresponding edges of the parent compounds [45, 46, 50]. Although the main features of Cu  $L_{3,2}$  XAS for  $A^5\text{Cr}_2\text{O}_4$  are quite similar to those of the parent  $\text{CuCr}_2\text{O}_4$ , the features at approximately 933.9 eV and 953.7 eV are more intense. This slight difference may be attributed to the differences in crystal field parameters due to the variation in local structures around Cu (demonstrated in the latter part of the manuscript). Overall, our XAS measurements further established a normal spinel structure similar to that of all the parent compounds. Fig. 2(f) shows the expected spin configurations for each of the cations of  $A^5\text{Cr}_2\text{O}_4$ , according to the oxidation state found by XAS. This is further corroborated by the

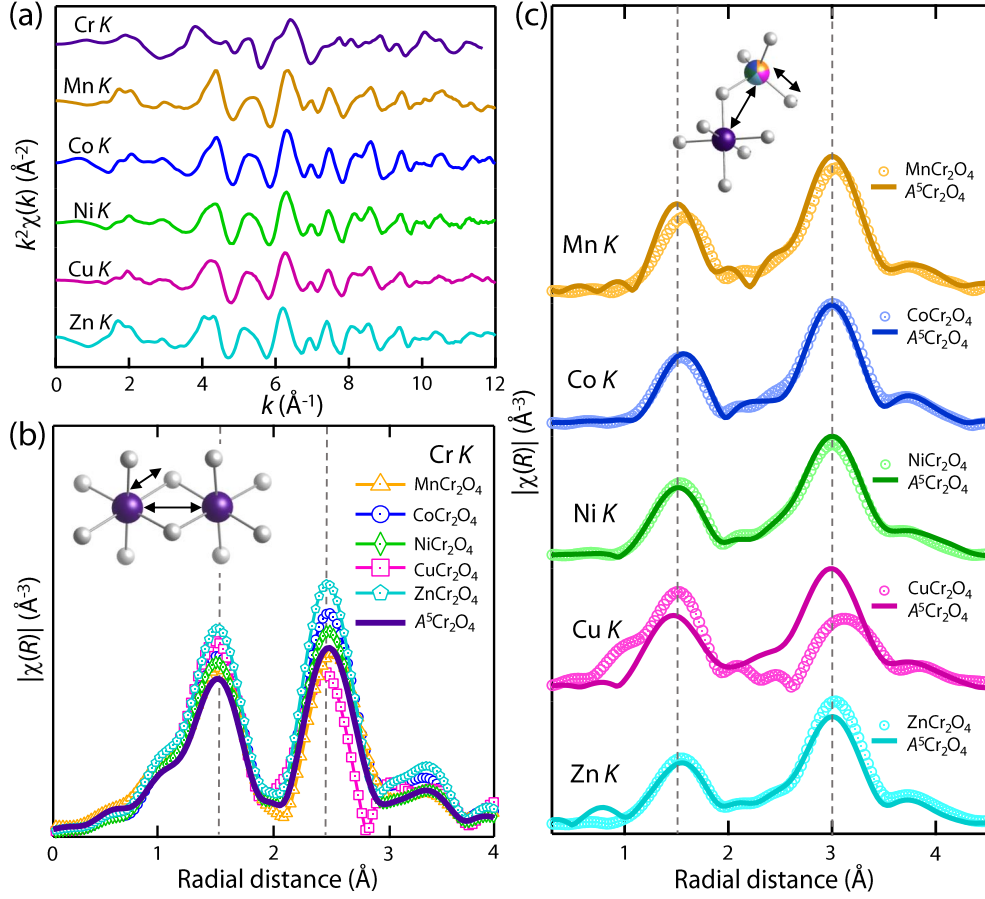


FIG. 3. **Probing the local structure using EXAFS.** **a** The  $k$  weighted EXAFS spectra in  $A^5Cr_2O_4$ . The Fourier transform of the EXAFS spectra at **b** Cr  $K$ -edge and **c**  $A$   $K$ -edges in the parent oxides and  $A^5Cr_2O_4$ . Inset panels show the first and second nearest neighbor distances (b) for Cr, (c) for  $A$  site.

Curie–Weiss analysis of magnetic susceptibility, which is discussed in the later section of the manuscript.

**Investigation of local distortions:** To investigate the local structural distortions around Cr, Mn, Co, Ni, Cu, and Zn, we recorded the  $K$ -edge EXAFS spectra. The spectra of every transition metal edge were calibrated using the corresponding standard metal foils. To avoid interference from the next absorption edge in  $A^5Cr_2O_4$ , the spectra were truncated above  $12 \text{ \AA}^{-1}$  in  $k$  space. Similar features across Mn, Co, Ni, Cu, and Zn  $K$ -edges [Fig. 3(a)] suggest a similar coordination geometry with a uniform distribution throughout the lattice. The Fourier transform (FT) of  $k^2 \cdot \chi(k)$  of Cr and  $A$   $K$ -edges for each of the parent compounds and  $A^5Cr_2O_4$  are shown in Fig. 3(b) and (c), respectively. The first peak at  $1.55 \text{ \AA}$  in both Cr and  $A$   $K$ -edge data suggests similar Cr-O



and A-O distances in  $A^5\text{Cr}_2\text{O}_4$  and parent compounds. The second peak at 2.5 Å in Cr  $K$ -edge data corresponds to Cr-Cr distance, while the one at 3 Å in  $A$   $K$ -edge data corresponds to A-Cr distance, implying different cation environments. We also note that the real scattering distance shifts by approximately 0.5 Å as the phase shift in the Fourier transform remains uncorrected.

The FT of  $k^2 \cdot \chi(k)$  for Cr  $K$  in  $A^5\text{Cr}_2\text{O}_4$  [Fig. 3(b)] shows similar features like the parent compounds (except  $\text{CuCr}_2\text{O}_4$ ). However, Fig. 3(c) reveals significant changes in local structures around Cu and Mn in  $A^5\text{Cr}_2\text{O}_4$  compared to  $\text{CuCr}_2\text{O}_4$  and  $\text{MnCr}_2\text{O}_4$ , respectively. This is likely due to the difference in crystal symmetry (cubic vs. tetragonal) and lattice volume changes. Local structures around Co, Ni, and Zn in  $A^5\text{Cr}_2\text{O}_4$  are similar to their parent compounds, except for a slight change in Zn-Cr distance.

To quantify the effect of all differences shown in Fig. 3, we performed fittings for the  $A$   $K$ -edge spectra ( $A = \text{Mn, Co, Ni, Cu}$  and  $\text{Zn}$ ) in every parent compound in the  $k$  range of 2 to 14 Å<sup>-1</sup> and the  $R$  range of 1 to 4.5 Å (details are in the Methods section). For the Cr  $K$ -edge, the  $k$  range of 2 to 12 Å<sup>-1</sup> and the  $R$  range of 1 to 3.7 Å were employed in fittings (see Fig. 4 (a) and Fig. S3 and Tables S2, S3, S4 in Supplementary). The analysis considered structural symmetries determined by XRD. In the cubic model, a Cr cation has 6 O anions as first neighbors (Fig. 4 (b)), 6 Cr cations as second neighbors (Fig. 4 (c)), and 6  $A$  cations as third neighbors (Fig. 4 (d)). In the tetragonal model, six equal bond lengths in each case split into equal bond distances with coordination four and two, whose weighted average is plotted (denoted by closed circles) for easier comparison (for  $\text{NiCr}_2\text{O}_4$  and  $\text{CuCr}_2\text{O}_4$ ). From the analysis, we could infer that the bond distances Cr-O (1.97 Å), Cr-Cr (2.96 Å) and Cr- $A$  (3.46 Å) in  $A^5\text{Cr}_2\text{O}_4$  are akin to that of  $\text{CoCr}_2\text{O}_4$ ,  $\text{ZnCr}_2\text{O}_4$  and also with the weighted average bond lengths of  $\text{NiCr}_2\text{O}_4$ . Consistent with the difference in lattice constant, these bond lengths are higher in  $\text{MnCr}_2\text{O}_4$ . Also, the average Cr-O and Cr- $A$  bond distances of  $\text{CuCr}_2\text{O}_4$  are lower compared to  $A^5\text{Cr}_2\text{O}_4$ . Unlike  $\text{CuCr}_2\text{O}_4$  and  $\text{NiCr}_2\text{O}_4$ , we observe a single type of Cr-O bond distance in  $A^5\text{Cr}_2\text{O}_4$ , indicating the absence of Jahn-Teller distortion within the detection limit of EXAFS. Our attempts to analyze Cr  $K$  EXAFS using a tetragonal symmetry yield unphysical fitting parameters (Table S5 in Supplementary). This contrasts sharply with Cu-containing rock-salt HEO, where local Jahn-Teller distortions survives [34, 51].

To further explore the possibility of Jahn-Teller like distortions around Cr, we employed DFT calculations for 10 different supercells with 448 atoms to address this. Random distributions of 12 Mn, 13 Co, 13 Ni, 13 Cu, and 13 Zn atoms were considered across the 64  $A$ -sites to generate these 10 distinct disordered structures (details of the calculations are in the Method section). Histogram

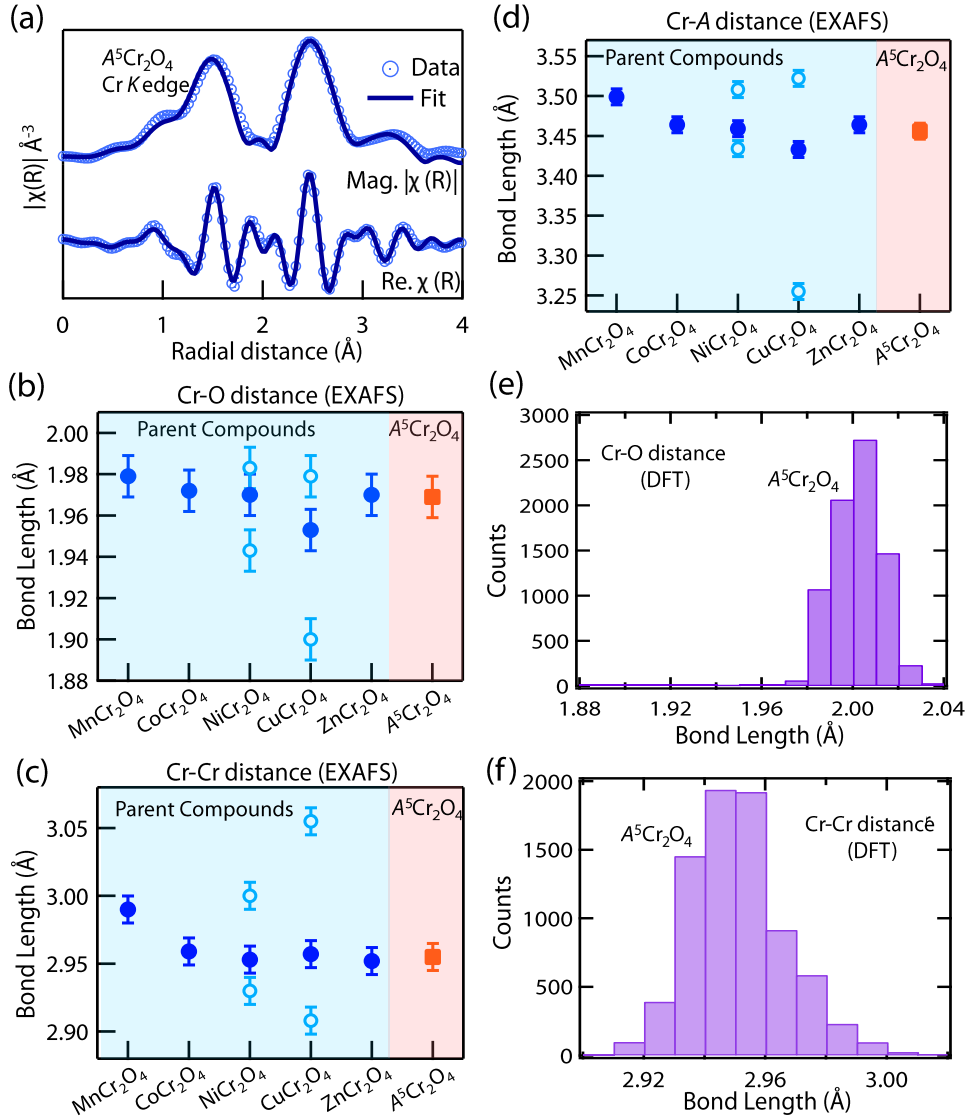
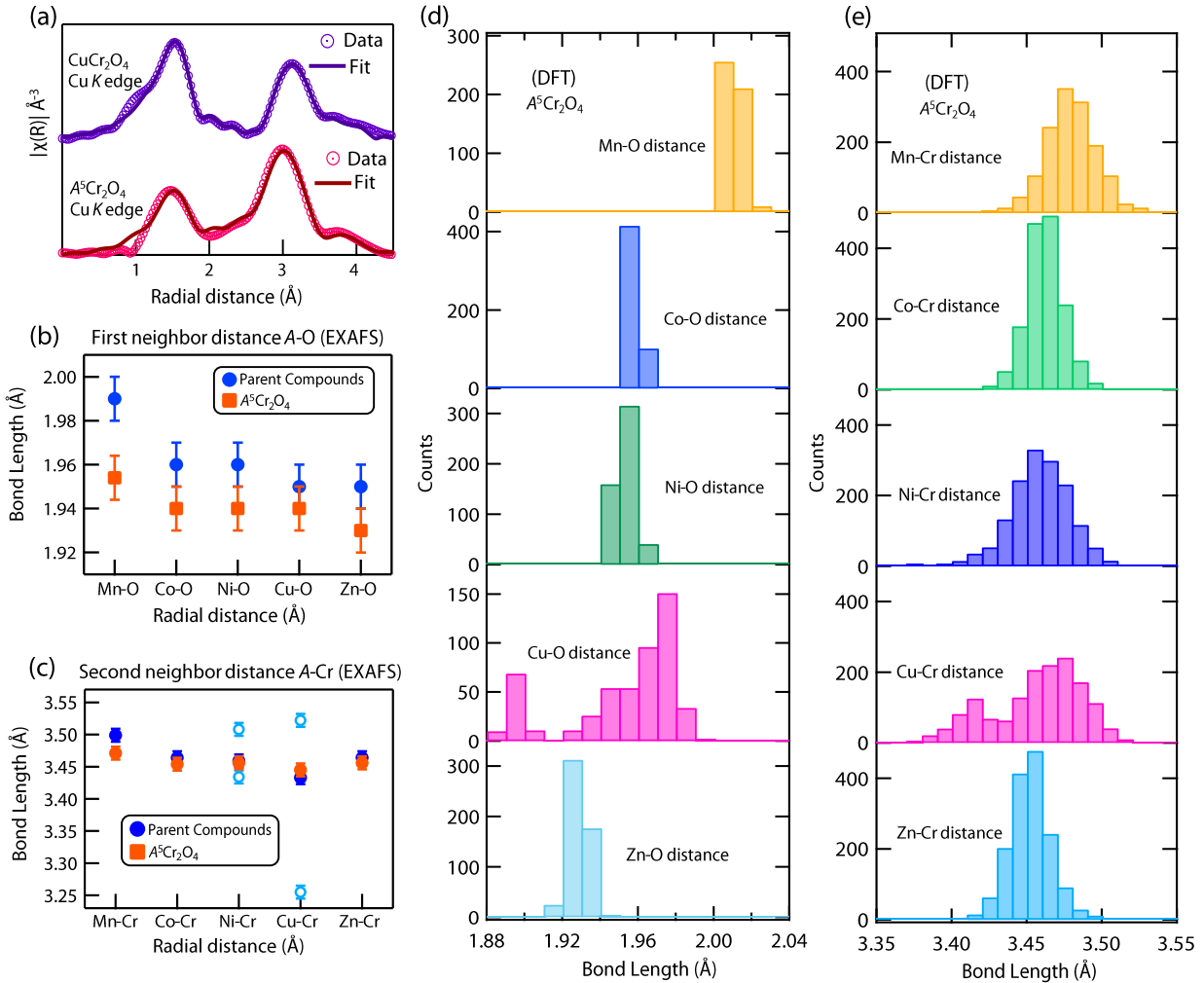


FIG. 4. **Analysis of local structure in the octahedral environment.** **a** The Fourier transformed EXAFS spectrum along with the fitted data [the magnitude  $|\chi(R)|$  and the real part  $Re. \chi(R)$ ] in  $A^5Cr_2O_4$ . The bond distances from Cr for first neighbor O, second neighbor Cr and third neighbor A ions are depicted in **[b-d]** as obtained from EXAFS fittings for every pristine chromite spinels and  $A^5Cr_2O_4$ . Due to Jahn-Teller distortion,  $NiCr_2O_4$  and  $CuCr_2O_4$  display two bond lengths (drawn as open circles), whose weighted average (denoted by the closed circle) is also plotted for ease of comparison. Histogram plots for **e** Cr-O, and **f** Cr-Cr bond lengths, obtained from DFT calculations of 10 different disordered structures.



**FIG. 5. Analysis of local structure in the tetrahedral environment.** The magnitude of the Fourier transformed EXAFS spectra along with fittings obtained at the **a** Cu  $K$ -edge in  $\text{CuCr}_2\text{O}_4$  and  $\text{A}^5\text{Cr}_2\text{O}_4$ . The bond lengths depicted in **[b-c]** are obtained from EXAFS fittings for every pristine chromite spinels and  $\text{A}^5\text{Cr}_2\text{O}_4$ . In **c**, due to Jahn-Teller distortion,  $\text{NiCr}_2\text{O}_4$ , and  $\text{CuCr}_2\text{O}_4$  display two bond lengths between  $A$  and Cr cations (drawn as open circles), whose weighted average (closed circle) is plotted for ease of comparison. Histogram plots for **d** first neighbor  $A$ -O, and **e** second neighbor  $A$ -Cr bond lengths, found from DFT calculations of 10 different disordered structures.

plots illustrating the distribution of Cr-O, Cr-Cr bond distances, obtained from the calculations of all ten structures, are presented in Fig. 4 (e), (f), respectively. While a small distribution of Cr-O bond distance ( $\sim 2.0 \pm 0.02$  Å) is found from the calculation, we do not find any Jahn-Teller distortions [DFT calculations with similar settings can provide Jahn-Teller distortions for

CuCr<sub>2</sub>O<sub>4</sub>, see Supplementary Table S6]. Cr-Cr bond distances also exhibit a distribution, with the peak position [Fig. 4 (f)] closely matching the EXAFS-derived value of A<sup>5</sup>Cr<sub>2</sub>O<sub>4</sub> [Fig. 4 (c)]. However, EXAFS cannot reveal precise distributional information due to its averaging of local environments around all Cr ions.

The fittings of *A*-site EXAFS analysis for parent ACr<sub>2</sub>O<sub>4</sub> are presented in Supplementary Fig. S3. The *A* ions share the same coordination for first-neighbor oxygen and fourth-neighbor *A* cation for both cubic and tetragonal structures. In case of cubic MnCr<sub>2</sub>O<sub>4</sub>, we find that Mn has 4 O at  $R = 1.99 \text{ \AA}$ , 12 O at  $R = 3.32 \text{ \AA}$ , 12 Cr at  $R = 3.50 \text{ \AA}$  and 4 Mn as at  $R = 3.64 \text{ \AA}$  as direct scatterers. The Mn-Cr distance is very similar to the distance evaluated independently from the fitting of Cr *K*-edge EXAFS. However, the third neighbor Mn-O distance appears lower than the Mn-Cr bond length, though Cr is the second neighbor of Mn according to the structure obtained from diffraction. We find this deviation for all six compounds and the previous EXAFS studies [52, 53]. This is likely caused by the weak *A*-O scattering contribution from the third neighbor due to oxygen's low atomic number. Thus, we will only focus on the first neighbor *A*-O and the second neighbor *A*-Cr distances in the remaining part of the paper. In the case of tetragonal CuCr<sub>2</sub>O<sub>4</sub>, the analysis of Cu *K*-edge finds 4 O at  $R = 1.95 \text{ \AA}$ , 8 O at  $R = 3.46 \text{ \AA}$  and 4 O at  $R = 3.04 \text{ \AA}$  8 Cr at  $R = 3.52 \text{ \AA}$  and 4 Cr at  $R = 3.26 \text{ \AA}$ , and 4 Cu at  $R = 3.61 \text{ \AA}$  as direct scatterers. All bond distances obtained from the fitting have been listed in Supplementary Tables S2, S3, and S4.

The EXAFS fittings of each *A*-site of A<sup>5</sup>Cr<sub>2</sub>O<sub>4</sub> were performed considering cubic symmetry in accordance with the XRD result. Excellent fitting has been found for each case, including Cu *K*-edge [Fig. 5 (a)] and Ni *K*-edge (see Supplementary Fig. S3 (c)). We have also attempted to fit Cu *K* EXAFS of A<sup>5</sup>Cr<sub>2</sub>O<sub>4</sub> using tetragonal symmetry, similar to the parent compound CuCr<sub>2</sub>O<sub>4</sub>. However, such fitting results in negative  $\sigma^2$  (see Supplementary Table S5) for Cu. The comparison of each neighbor distance among the pristine members and doped compound reveals several interesting trends (Fig. 5 (b) and (d)). The Mn-O distance in MnCr<sub>2</sub>O<sub>4</sub> is the largest due to its bigger unit cell volume than other pristine materials. In A<sup>5</sup>Cr<sub>2</sub>O<sub>4</sub>, the first neighbor *A*-O distance depends on the specific element positioned at the *A*-site. The Co-O, Ni-O, and Cu-O distances are very similar, whereas Mn-O and Zn-O distances differ. Notably, the *A*-O bond distances are smaller than those in the corresponding parent ACr<sub>2</sub>O<sub>4</sub>, indicating that these local variations are not simply due to changes in the overall crystal volume. Furthermore, second neighbor *A*-Cr distances [Fig. 5(c)], determined from *A*-site EXAFS in A<sup>5</sup>Cr<sub>2</sub>O<sub>4</sub>, vary mildly with the specific *A* cation. The fourth neighbor *A*-*A* distance is found to be  $\simeq 3.58 \pm 0.02 \text{ \AA}$  in the fittings of each *A*-

site EXAFS [see Supplementary Tables S2, S3 and S4]. This is comparable to those in  $\text{CoCr}_2\text{O}_4$ ,  $\text{NiCr}_2\text{O}_4$ , and  $\text{ZnCr}_2\text{O}_4$ , but smaller to the ones in  $\text{MnCr}_2\text{O}_4$ , and  $\text{CuCr}_2\text{O}_4$ .

Next, we discuss  $A$ -site bond lengths in  $A^5\text{Cr}_2\text{O}_4$  from the same DFT calculations used to generate Fig. 4 (e)-(f) for Cr sites. The histogram plots for first neighbor  $A$ -O distances and second neighbor  $A$ -Cr distances from DFT calculations have been presented in Fig. 5 (e), and (f), respectively. Despite, the consideration of ten different disordered structures in our calculations, Mn-O, Co-O, Ni-O and Zn-O distances do not exhibit any statistical distribution, implying they maintain a specific bond length. In sharp contrast, Cu-O bond distances display a wide range of values. The trend in the magnitude of these  $A$ -O bond distances is also found to be very similar to what we observe from the EXAFS: Mn-O bond being the longest and Zn-O being the shortest. Interestingly, the second neighbour Mn-Cr, Co-Cr, Ni-Cr, and Zn-Cr also exhibit a distribution [Fig. 5 (e)], with their peak positions similar to the Cr- $A$  distance obtained from EXAFS [Fig. 5 (c)]. Moreover, the distribution width for Cu-Cr bond is broader than the other  $A$ -Cr bonds, which is also consistent with our findings of higher  $\sigma^2$  (mean square variation of bond length) for Cu-Cr distances compared to other  $A$ -Cr bonds in  $A$  sites EXAFS fittings of  $A^5\text{Cr}_2\text{O}_4$  (Table S4 in Supplementary)

Our combined EXAFS and DFT analysis reveal that the element-specific structural distortions in  $A^5\text{Cr}_2\text{O}_4$  extend beyond the first neighbor shell of  $A$  sites. The broad distribution of Cu-O bond distances and specific value of other  $A$ -O distances signifies that the element-specific local distortions are accommodated primarily by the highly flexible  $\text{CuO}_4$  tetrahedral units. The connection between  $\text{CuO}_4$  tetrahedral and  $\text{CrO}_6$  octahedra through a common oxygen (inset of Fig. 3 (c)) results in a broad distribution of Cr-Cu distances, while Cr-O and Cr-Cr distances exhibit a narrower spread without any Jahn-Teller distortion. Additionally, each  $\text{CrO}_6$  octahedron is connected to another five  $\text{AO}_4$  units ( $A = \text{Mn, Co, Ni, Cu, Zn}$ ), contributing to narrower distributions for other Cr- $A$  bond lengths.

**Correlation between structural distortions and magnetic interaction:** These bond lengths are expected to play a crucial role in comprehending the strength of magnetic interactions in  $A\text{Cr}_2\text{O}_4$  spinels. The theory of ground state magnetic configuration of cubic  $AB_2\text{O}_4$  is very often described by the following Hamiltonian with classical Heisenberg spins considering  $B$ - $B$ , and  $A$ - $B$  exchanges, initially proposed by Lyons, Kaplan, Dwight, and Menyuk [38, 54, 55].

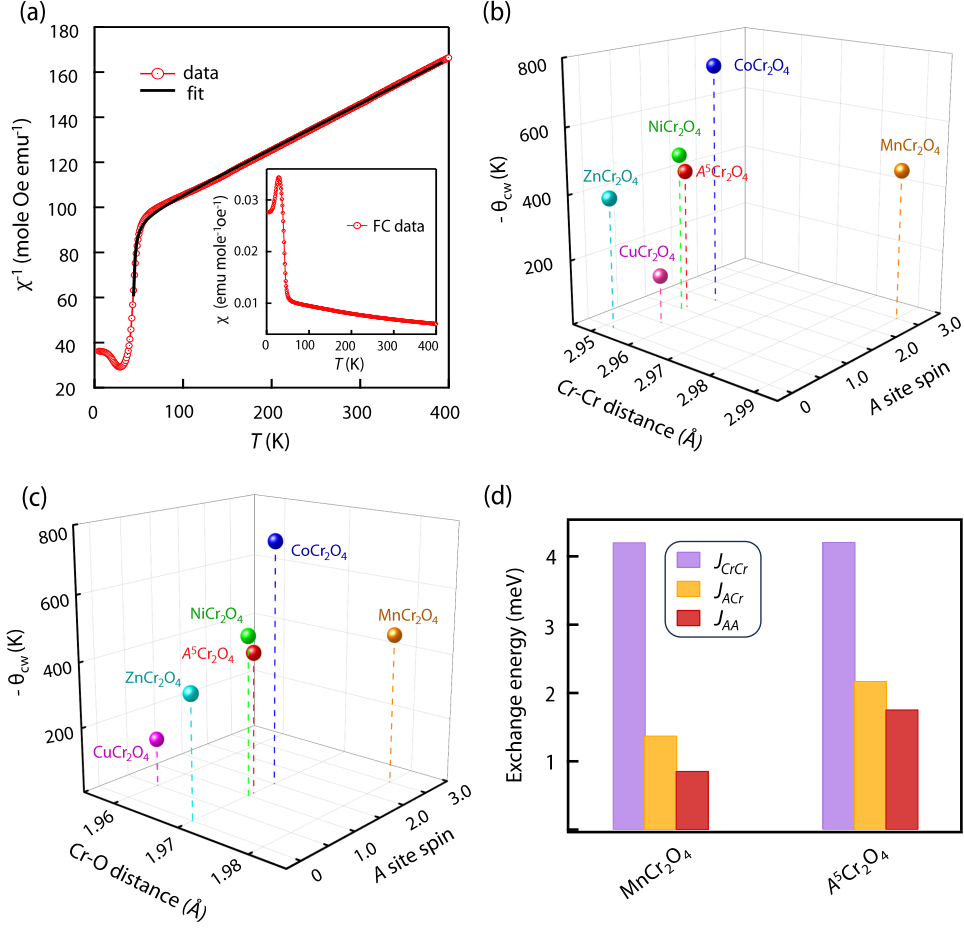


FIG. 6. **Magnetic characterization and its connection with local structure** **a** Fitting of inverse magnetic dc susceptibility using Curie-Weiss equation above  $T_N$  in  $A^5Cr_2O_4$  at 5000 Oe. Inset features field cooled (FC) dc susceptibility as a function of temperature.  $-\theta_{CW}$  is plotted as a function of **b** Cr-Cr bond distance and  $A$ -site spin and **c** Cr-O bond distance and  $A$  site spin in parent oxides and  $A^5Cr_2O_4$ . **d** A comparison of the magnetic exchange interaction energy between two Cr cations ( $J_{CrCr}$ ), between Cr and  $A$  ( $J_{ACr}$ ), and between two  $A$  cations ( $J_{AA}$ ) in  $MnCr_2O_4$  and  $A^5Cr_2O_4$ .

$$H = 2J_{AB}S_A S_B \left( \sum_{\langle ij \rangle} \vec{\sigma}_i^A \cdot \vec{\sigma}_j^B + \frac{3u}{4} \sum_{\langle ij \rangle} \vec{\sigma}_i^B \cdot \vec{\sigma}_j^B \right) \quad (1)$$

The sums are over nearest-neighbor  $A$ - $B$  and  $B$ - $B$  pairs and the parameter  $u = \frac{4J_{BB}S_B}{3J_{AB}S_A}$  and  $\vec{\sigma}_j^\alpha = \vec{S}_j^\alpha / S_j^\alpha$  with  $\alpha=A$  and  $B$ . The interaction within the diamond sublattice ( $J_{AA}$ ) has also been claimed to be important in recent studies [56, 57]. In chromite spinels, the magnetic interaction

between two Cr is a direct exchange and thus depends strongly on the Cr-Cr distance [56]. The superexchange between  $A$  and Cr is mediated through interconnecting oxygen, and the strength will depend on the bond lengths  $A$ -O and Cr-O,  $A$ -O-Cr bond angle, and the electronic configuration of  $A$  site ions. Due to the presence of four different magnetic ions ( $Zn^{2+}$  is non-magnetic) at the  $A$  site of  $A^5Cr_2O_4$ , there would be ten types  $J_{AA}$  and four types of  $J_{ACr}$  interactions. Interestingly, a direct dependence of magnetic transition temperatures on the average crystal structure of perovskite HEOs has been demonstrated, even though the details of the magnetic features within the magnetically ordered phase are more complicated [58–62]. In the case of parent  $ACr_2O_4$  members, the magnetic frustration caused by antiferromagnetic Cr-Cr interactions within the pyrochlore sublattice varies, resulting in a very reduced magnetic ordering temperature compared to the Curie-Weiss temperature ( $\theta_{CW}$ ) (Supplementary Table S7). As  $\theta_{CW}$  is a measure of molecular field and considered as an approximate indicator of the strength of mean-field magnetic interaction between the ions [63], we have focused on finding out any relation between  $\theta_{CW}$  and the bond lengths at 300 K obtained from the EXAFS analysis.

The temperature-dependent magnetic susceptibility [ $\chi=M/H$ ] for  $A^5Cr_2O_4$ , measured under a magnetic field ( $H$ ) of 5000 Oe in field cooled condition has been depicted as an inset of Fig. 6 (a). We found a magnetic transition around 50 K. The main panel represents the fitting of the inverse of dc susceptibility at high temperature using molecular field theory of a ferrimagnet [64]

$$\chi^{-1} = \frac{T - \theta_{CW}}{C_A + 2C_B} - \frac{C''}{T - \theta'} \quad (2)$$

The first term is the hyperbolic high-temperature linear part with a Curie-Weiss form, where  $C_A$  and  $C_B$  correspond to Curie constants related to the two magnetic sublattices  $M_A$  and  $M_B$ , respectively.  $\theta_{CW}$  is the Curie-Weiss temperature. The second term is the hyperbolic low- $T$  asymptote, where  $C''$  and  $\theta'$  are constants akin to different Weiss coefficients that represent the inter and intrasublattice interactions. From this fitting, we have obtained a Curie-Weiss temperature of  $\theta_{CW} = -432$  K and the effective magnetic moment of  $6.33 \mu_B/f.u.$  using the formula  $\mu_{eff} = \sqrt{\frac{3K_B(C_A+2C_B)}{N_A}}$  [65], where  $K_B$  is Boltzmann's constant and  $N_A$  is Avogadro's number. Interestingly,  $\mu_{eff}$  is very similar to the expected value of  $6.26 \mu_B/f.u.$ , calculated by considering the average magnetic moments of  $A^{2+}$  ( $A = Mn, Co, Ni, Cu$ ;  $Zn^{2+}$  is nonmagnetic) and  $Cr^{3+}$  of  $A^5Cr_2O_4$  ( $\mu_{eff} = \sqrt{2\mu_{Cr}^2 + \mu_A^2}$ ). The most surprising finding is that despite having a series of magnetic interactions [Cr- $A$  and  $A$ - $A'$  with  $A, A' = Mn, Co, Ni, Cu$ ], the  $\theta_{CW}$  of  $A^5Cr_2O_4$  is comparable to  $NiCr_2O_4$  [43] (also see Supplementary Figure S4) and  $MnCr_2O_4$  [56]. The effective

magnetic moment also closely resembles  $\text{NiCr}_2\text{O}_4$  ( $6.64 \mu_B/\text{f.u.}$ ). These findings also indicate that the net magnetic interaction, felt by a magnetic ion in CCO, can be treated using a mean-field approach.

To understand the effect of local distortions on magnetism,  $|\theta_{\text{CW}}|$  for all six compounds have been plotted as a function of EXAFS derived bond lengths and the  $A$ -site spin value in Fig. 6(b), (c). The  $\theta_{\text{CW}}$  of the parent compounds  $A\text{Cr}_2\text{O}_4$  is obtained from Ref. [43, 56, 66] and an average of  $A$ -site spin ( $S_A=1.1$ ) for  $A^5\text{Cr}_2\text{O}_4$  has been considered for these plots. The Cr-Cr bond length (Fig.6 (b)) is considered as it corresponds to the Cr-Cr direct exchange. The Cr-O bond length is also plotted in connection with the  $A$ -O-Cr superexchange path (Fig.6 (b)). While the  $A$ -O bond length also plays a role in  $A$ -O-Cr superexchange strength, we were unable to create a similar plot for  $A$ -O bond lengths because this distance depends on the specific atom occupying the  $A$ -site in  $A^5\text{Cr}_2\text{O}_4$ . The  $\theta_{\text{CW}}$  of  $A^5\text{Cr}_2\text{O}_4$  is closer to the value of  $\text{NiCr}_2\text{O}_4$  and  $\text{MnCr}_2\text{O}_4$ . We have further evaluated the mean-field magnetic exchange parameters from our magnetization data, following the process described in Ref. [56] [also see Supplementary]. The exchange interaction parameters  $J_{BB}$  (interactions between two  $\text{Cr}^{3+}$ ),  $J_{AB}$  (between  $A^{2+}$  and  $\text{Cr}^{3+}$ ), and  $J_{AA}$  (between two  $A^{2+}$  cations) have been compared in Fig. 6(d). The exchange parameters for  $\text{MnCr}_2\text{O}_4$  have been adapted from Ref. [56]. Interestingly, the  $J_{BB}$  interaction shows almost no difference between these compounds. However, the  $J_{AB}$  and  $J_{AA}$  values for  $A^5\text{Cr}_2\text{O}_4$  are higher than those of  $\text{MnCr}_2\text{O}_4$ . The extraction of these  $J$ s using equation 2 is not possible for  $\text{NiCr}_2\text{O}_4$  due to an anomaly in the magnetic susceptibility at the cubic-to-tetragonal transition ( $\sim 315$  K, see Supplementary Fig S4). However, Fig.6 (b) and (c) clearly demonstrate the close similarity between  $A^5\text{Cr}_2\text{O}_4$  and  $\text{NiCr}_2\text{O}_4$  in terms of key parameters like Cr-Cr distance, Cr-O distance, and  $A$ -site spin and  $\theta_{\text{CW}}$ . This strong resemblance highlights the crucial role of local bond lengths around the Cr ions in determining the mean-field magnetic interactions within  $A^5\text{Cr}_2\text{O}_4$ .

**Conclusions:** We have synthesized a compositionally complex spinel oxide  $A^5\text{Cr}_2\text{O}_4$ , with  $\text{Cr}^{3+}$  ions occupying the octahedral site and a uniform distribution of  $A^{2+}$  ( $A = \text{Mn, Co, Ni, Cu, and Zn}$ ) ions in the tetrahedral site. Our investigation of the local structure employing element-specific EXAFS analysis and DFT calculations with various disordered configurations reveals several unique features that distinguish it from previously reported high entropy oxides. Unlike HEOs with rock-salt structures [34, 51], where local Jahn-Teller distortions around  $\text{Cu}^{2+}$  ions are typically preserved, our study reveals a complete absence of such distortions in  $A^5\text{Cr}_2\text{O}_4$ . In contrast to other HEOs, where local distortions are limited to the first nearest neighbors of the doped



cations [34, 35], in the present study,  $A^5\text{Cr}_2\text{O}_4$  exhibits variation in local distortions extending beyond the first neighbors. Despite a broad distribution of Cu-O bond distances, other A-O distances acquire specific values, implying the high flexibility of  $\text{CuO}_4$  tetrahedral units to maintain an overall cubic structure by adjusting their positions. Such adjustment also leads to a broad distribution of second neighboring Cu-Cr distances and a narrow distribution of other A-Cr, Cr-Cr and Cr-O bond lengths. Despite substantial local distortions, the mean-field magnetic interaction energies of  $A^5\text{Cr}_2\text{O}_4$  are remarkably similar to those of  $\text{NiCr}_2\text{O}_4$  due to their closely matched average A-site spin value, as well as their average Cr-O and Cr-Cr bond lengths.

Unveiling the temperature dependence of  $A^5\text{Cr}_2\text{O}_4$ 's long-range and local structures presents a compelling avenue for future research as some of the constituent members undergo structural transitions below room temperature [43]. Future investigations into the spin arrangements and potential multiferroic phases are warranted. Furthermore, we believe that our approach, which compares EXAFS analysis of CCO with the constituent parent members along with the DFT calculations for a set of disordered configurations, would be a powerful tool for revealing subtle details regarding structural modifications in other compositionally complex materials.

## Methods

**Experimental details:** Polycrystalline samples of five parent compounds  $A\text{Cr}_2\text{O}_4$  ( $A = \text{Mn}, \text{Co}, \text{Ni}, \text{Cu}$  and  $\text{Zn}$ ) were synthesized by conventional solid-state synthesis with a stoichiometric amount of  $\text{Cr}_2\text{O}_3$  and AO. The first heating was carried out at  $900^\circ\text{C}$ , followed by a second heat treatment at  $1300^\circ\text{C}$  with intermediate grindings. The annealing of  $\text{MnCr}_2\text{O}_4$  and  $\text{CuCr}_2\text{O}_4$  were performed in argon and oxygen atmosphere, respectively, while the rest of the compounds were heated in air. The  $A^5\text{Cr}_2\text{O}_4$  was synthesized in a similar route in the air. The sample purity of all samples was checked by powder XRD using a laboratory-based Rigaku Smartlab diffractometer. The final XRD patterns were further refined by the Rietveld method using the FULLPROF suite [67]. The Raman spectra were recorded using Confocal Photoluminescence Raman Spectro Microscope. Data was collected using 532 nm LASER and 1800 rules/mm grating in  $100\text{-}800\text{ cm}^{-1}$  wavenumber range. The temperature-dependent magnetization measurement was carried out in the range of 5 K to 400 K using a commercial SQUID-VSM MPMS from M/s Quantum Design, USA. XAS spectra for  $L_{3,2}$  edges of Cr, Mn, Co, Ni, Cu of the  $A^5\text{Cr}_2\text{O}_4$  were recorded in total electron yield mode at the beamline 4.0.2 of the Advanced Light Source, USA. Ni  $L_{3,2}$  edge

of  $\text{NiCr}_2\text{O}_4$  and Cu  $L_{3,2}$  edge of  $\text{CuCr}_2\text{O}_4$  were also measured.

EXAFS measurements for all transition metal  $K$ -edge for all five parent compounds and  $A^5\text{Cr}_2\text{O}_4$  have been performed at the P65 beamline, PETRA III Synchrotron Source (DESY, Hamburg, Germany) and at beamline 20-BM of the Advanced Photon Source, USA. For EXAFS experiments in transmission geometry, the absorbers were prepared by uniformly coating the powder samples on scotch tape. The incident and the transmitted photon energies were simultaneously recorded using the gas ionization chambers as detectors. At each  $K$ -edge, at least three scans were collected to average the statistical noise. The analysis was carried out using well-established procedures in the DEMETER suite [68].

For the EXAFS fittings, the amplitude reduction factor  $S_0^2$  and correction to the edge energy  $\Delta E_0$  were derived from the analysis of the corresponding standard metal spectra, and these parameters were kept fixed throughout the analysis. The parameters consisting of correction to the bond length  $\Delta R$  and mean square variation in bond length  $\sigma^2$  were varied for each scattering path. For the cubic model, ten and eight independent parameters were used in the fittings of  $A$   $K$ -edge and Cr  $K$ -edge spectra, respectively. Fourteen independent parameters were used for the tetragonal model to fit both Cr  $K$  and  $A$   $K$ -edges. In the case of  $\text{NiCr}_2\text{O}_4$ , the number of independent parameters was similar to the cubic model due to the very weak tetragonal distortion.

For  $A^5\text{Cr}_2\text{O}_4$ , a model describing a normal cubic spinel structure was modified to incorporate a solid solution containing equal amounts of Mn, Co, Ni, Cu and Zn at the tetrahedral site. The coordination numbers were constrained to maintain consistency with the cubic spinel structure. A realistic solution-like distribution was simulated for both tetrahedral and octahedral sites by randomly dividing the concerned coordination shell among the five  $A$  cations. Furthermore, the five cations were confined to a specific distance from the absorber, independent of the species. The R factor for every fit was less than 2%, indicating the reliability of the fitting outcomes.

**DFT calculations:** A cubic spinel structure of  $A^5\text{Cr}_2\text{O}_4$  was utilized to generate ten different random oxide supercells of  $2 \times 2 \times 2$  dimensions, consisting of 448 atoms (64  $A$ , 128 Cr, and 256 O atoms). To form the random distribution, 12 Mn, 13 Co, 13 Ni, 13 Cu, and 13 Zn atoms were distributed among the 64 available  $A$  sites. Each of the ten random oxides was created by randomly rearranging the  $A$  sites while keeping the number of each type of atom constant. We conducted structural optimization using the Vienna Ab initio Simulation Package (VASP) based on plane wave basis set and projector augmented wave pseudopotentials [69, 70]. The POSCAR files of the ten different structures have been supplied as a separate file along with the manuscript. The

exchange-correlation potential was described using the generalized gradient approximation (GGA) with the Perdew, Burke, and Ernzerhof (PBE) functional [71]. A static Hubbard correction was effectively applied to account for localized Coulomb interactions in highly correlated 3d transition metals, following the Dudarev approach [72]. The  $U_{eff}$  values were set to 4.0, 3.0, 5.0, 8.0, 8.0, and 3.0 eV for Mn, Co, Ni, Cu, Zn, and Cr, respectively, in line with the reported values for transition metal oxides [73–76]. This setup resulted in a good agreement in bond lengths between experimental data and DFT calculations. For Brillouin zone integration, a Gamma-centered  $1 \times 1 \times 1$  k-point grid was employed. The lattice constants were determined based on experimental results. The equilibrium atomic positions were obtained via energy minimization, employing the conjugate gradient method until the force components on each atom fell below 0.01 eV/Å.

## DATA AVAILABILITY

All data are available from the corresponding authors upon reasonable request,

---

\* Contributed equally; [rukmagurudas@iisc.ac.in](mailto:rukmagurudas@iisc.ac.in)

† Contributed equally

‡ [smiddey@iisc.ac.in](mailto:smiddey@iisc.ac.in)

- [1] George, E. P., Raabe, D. & Ritchie, R. O. High-entropy alloys. *Nature reviews materials* **4**, 515–534 (2019).
- [2] Sarkar, A. *et al.* High-entropy oxides: fundamental aspects and electrochemical properties. *Advanced materials* **31**, 1806236 (2019).
- [3] Oses, C., Toher, C. & Curtarolo, S. High-entropy ceramics. *Nature Reviews Materials* **5**, 295–309 (2020).
- [4] Musicó, B. L. *et al.* The emergent field of high entropy oxides: Design, prospects, challenges, and opportunities for tailoring material properties. *APL Materials* **8**, 040912 (2020). URL <https://doi.org/10.1063/5.0003149>. [https://pubs.aip.org/aip/apm/article-pdf/doi/10.1063/5.0003149/14563544/040912\\_1\\_online.pdf](https://pubs.aip.org/aip/apm/article-pdf/doi/10.1063/5.0003149/14563544/040912_1_online.pdf).
- [5] Brahlek, M. *et al.* What is in a name: Defining “high entropy” oxides. *APL Materials* **10**, 110902 (2022). URL <https://doi.org/10.1063/5.0122727>. <https://pubs.aip.org/aip/apm/article->

pdf/doi/10.1063/5.0122727/16490715/110902\_1\_online.pdf.

- [6] Kotsonis, G. N. *et al.* High-entropy oxides: Harnessing crystalline disorder for emergent functionality. *Journal of the American Ceramic Society* **106**, 5587–5611 (2023).
- [7] Mazza, A. R. *et al.* Embracing disorder in quantum materials design. *Applied Physics Letters* **124**, 230501 (2024). URL <https://doi.org/10.1063/5.0203647>. [https://pubs.aip.org/aip/apl/article-pdf/doi/10.1063/5.0203647/19978559/230501\\_1\\_5.0203647.pdf](https://pubs.aip.org/aip/apl/article-pdf/doi/10.1063/5.0203647/19978559/230501_1_5.0203647.pdf).
- [8] Cantor, B., Chang, I., Knight, P. & Vincent, A. Microstructural development in equiatomic multicomponent alloys. *Materials Science and Engineering: A* **375**, 213–218 (2004).
- [9] Yeh, J.-W. *et al.* Nanostructured high-entropy alloys with multiple principal elements: novel alloy design concepts and outcomes. *Advanced engineering materials* **6**, 299–303 (2004).
- [10] Rost, C. M. *et al.* Entropy-stabilized oxides. *Nature communications* **6**, 8485 (2015).
- [11] Djenadic, R. *et al.* Multicomponent equiatomic rare earth oxides. *Materials Research Letters* **5**, 102–109 (2017).
- [12] Jiang, S. *et al.* A new class of high-entropy perovskite oxides. *Scripta Materialia* **142**, 116–120 (2018).
- [13] Sharma, Y. *et al.* Single-crystal high entropy perovskite oxide epitaxial films. *Physical Review Materials* **2**, 060404 (2018).
- [14] Patel, R. K. *et al.* Epitaxial stabilization of ultra thin films of high entropy perovskite. *Applied Physics Letters* **116**, 071601 (2020).
- [15] Brahlek, M. *et al.* Unexpected crystalline homogeneity from the disordered bond network in  $\text{La}(\text{Cr}_{0.2}\text{Mn}_{0.2}\text{Fe}_{0.2}\text{Co}_{0.2}\text{Ni}_{0.2})\text{O}_3$  films. *Phys. Rev. Mater.* **4**, 054407 (2020). URL <https://link.aps.org/doi/10.1103/PhysRevMaterials.4.054407>.
- [16] Musicó, B. *et al.* Tunable magnetic ordering through cation selection in entropic spinel oxides. *Phys. Rev. Mater.* **3**, 104416 (2019). URL <https://link.aps.org/doi/10.1103/PhysRevMaterials.3.104416>.
- [17] Sharma, Y. *et al.* Magnetic texture in insulating single crystal high entropy oxide spinel films. *ACS applied materials & interfaces* **13**, 17971–17977 (2021).
- [18] Johnstone, G. H. *et al.* Entropy engineering and tunable magnetic order in the spinel high-entropy oxide. *Journal of the American Chemical Society* **144**, 20590–20600 (2022).
- [19] Wright, A. J. *et al.* Size disorder as a descriptor for predicting reduced thermal conductivity in medium-and high-entropy pyrochlore oxides. *Scripta Materialia* **181**, 76–81 (2020).

- [20] Jiang, B. *et al.* Probing the local site disorder and distortion in pyrochlore high-entropy oxides. *Journal of the American Chemical Society* **143**, 4193–4204 (2020).
- [21] Kinsler-Fedon, C. *et al.* Synthesis, characterization, and single-crystal growth of a high-entropy rare-earth pyrochlore oxide. *Phys. Rev. Mater.* **4**, 104411 (2020). URL <https://link.aps.org/doi/10.1103/PhysRevMaterials.4.104411>.
- [22] Sarkar, A. *et al.* High entropy oxides for reversible energy storage. *Nature communications* **9**, 3400 (2018).
- [23] Chen, H. *et al.* Entropy-stabilized metal oxide solid solutions as co oxidation catalysts with high-temperature stability. *Journal of Materials Chemistry A* **6**, 11129–11133 (2018).
- [24] Braun, J. L. *et al.* Charge-induced disorder controls the thermal conductivity of entropy-stabilized oxides. *Advanced materials* **30**, 1805004 (2018).
- [25] Kante, M. V. *et al.* A high entropy oxide as high-activity electrocatalyst for water oxidation. *ACS Nano* **17**, 5329 (2023). URL <https://pubs.acs.org/doi/10.1021/acsnano.2c08096>.
- [26] Patel, R. K. *et al.* Thickness dependent OER electrocatalysis of epitaxial thin film of high entropy oxide. *Applied Physics Reviews* **10**, 031407 (2023). URL <https://doi.org/10.1063/5.0146005>. [https://pubs.aip.org/aip/apr/article-pdf/doi/10.1063/5.0146005/18068792/031407\\_1\\_5.0146005.pdf](https://pubs.aip.org/aip/apr/article-pdf/doi/10.1063/5.0146005/18068792/031407_1_5.0146005.pdf).
- [27] Zhao, B. *et al.* High-entropy enhanced microwave attenuation in titanate perovskites. *Advanced Materials* **35**, 2210243 (2023).
- [28] Schweidler, S. *et al.* High-entropy materials for energy and electronic applications. *Nature Reviews Materials* 1–16 (2024).
- [29] Moniri, S. *et al.* Three-dimensional atomic structure and local chemical order of medium-and high-entropy nanoalloys. *Nature* **624**, 564–569 (2023).
- [30] Aamlid, S. S., Oudah, M., Rottler, J. & Hallas, A. M. Understanding the role of entropy in high entropy oxides. *Journal of the American Chemical Society* **145**, 5991–6006 (2023).
- [31] Ruffoni, M., Pettifer, R., Pascarelli, S., Trapananti, A. & Mathon, O. Probing atomic displacements with thermal differential exafs. *Journal of Synchrotron Radiation* **14**, 421–425 (2007).
- [32] Newville, M. Fundamentals of xafs. *Reviews in Mineralogy and Geochemistry* **78**, 33–74 (2014).
- [33] Rehr, J. J. & Albers, R. C. Theoretical approaches to x-ray absorption fine structure. *Rev. Mod. Phys.* **72**, 621–654 (2000). URL <https://link.aps.org/doi/10.1103/RevModPhys.72.621>.

- [34] Rost, C. M., Rak, Z., Brenner, D. W. & Maria, J.-P. *Journal of the American Ceramic Society* **100**, 2732–2738 (2017).
- [35] Pu, Y. *et al.* (mg, mn, fe, co, ni) o: A rocksalt high-entropy oxide containing divalent mn and fe. *Science Advances* **9**, eadi8809 (2023).
- [36] D’Ippolito, V., Andreozzi, G. B., Bersani, D. & Lottici, P. P. Raman fingerprint of chromate, aluminate and ferrite spinels. *Journal of Raman Spectroscopy* **46**, 1255–1264 (2015).
- [37] Takubo, K. *et al.* Evolution of phonon raman spectra with orbital ordering in spinel  $\text{mnv}_2\text{O}_4$ . *Phys. Rev. B* **84**, 094406 (2011). URL <https://link.aps.org/doi/10.1103/PhysRevB.84.094406>.
- [38] Tsurkan, V., Von Nidda, H.-A. K., Deisenhofer, J., Lunkenheimer, P. & Loidl, A. On the complexity of spinels: Magnetic, electronic, and polar ground states. *Physics Reports* **926**, 1–86 (2021).
- [39] Tomiyasu, K., Fukunaga, J. & Suzuki, H. Magnetic short-range order and reentrant-spin-glass-like behavior in  $\text{co cr}_2\text{O}_4$  and  $\text{mn cr}_2\text{O}_4$  by means of neutron scattering and magnetization measurements. *Physical Review B* **70**, 214434 (2004).
- [40] Bhowmik, R., Ranganathan, R. & Nagarajan, R. Lattice expansion and noncollinear to collinear ferrimagnetic order in a  $\text{mn cr}_2\text{O}_4$  nanoparticle. *Physical Review B* **73**, 144413 (2006).
- [41] Yamasaki, Y. *et al.* Magnetic reversal of the ferroelectric polarization in a multiferroic spinel oxide. *Physical review letters* **96**, 207204 (2006).
- [42] Dey, K., Majumdar, S. & Giri, S. Ferroelectricity in spiral short-range-ordered magnetic state of spinel  $\text{mncr}_2\text{O}_4$ : Significance of topological frustration and magnetoelastic coupling. *Physical Review B* **90**, 184424 (2014).
- [43] Suchomel, M. R., Shoemaker, D. P., Ribaud, L., Kemei, M. C. & Seshadri, R. Spin-induced symmetry breaking in orbitally ordered  $\text{nicr}_2\text{O}_4$  and  $\text{cucr}_2\text{O}_4$ . *Physical Review B* **86**, 054406 (2012).
- [44] Dutton, S. E., Huang, Q., Tchernyshyov, O., Broholm, C. & Cava, R. J. Sensitivity of the magnetic properties of the  $\text{zn cr}_2\text{O}_4$  and  $\text{mg cr}_2\text{O}_4$  spinels to nonstoichiometry. *Physical Review B* **83**, 064407 (2011).
- [45] Van Der Laan, G., Chopdekar, R., Suzuki, Y. & Arenholz, E. Strain-induced changes in the electronic structure of  $\text{mncr}_2\text{O}_4$  thin films probed by x-ray magnetic circular dichroism. *Physical review letters* **105**, 067405 (2010).
- [46] Kim, I. *et al.* Electric polarization enhancement in multiferroic  $\text{cocr}_2\text{O}_4$  crystals with cr-site mixing. *Applied Physics Letters* **94** (2009).

- [47] Shannon, R. t. & Prewitt, C. Revised values of effective ionic radii. *Acta Crystallographica Section B: Structural Crystallography and Crystal Chemistry* **26**, 1046–1048 (1970).
- [48] Krysko, E. *et al.* Studies on the structure and the magnetic properties of high-entropy spinel oxide (mgmfnfeconi) al<sub>2</sub>o<sub>4</sub>. *APL Materials* **11**, 101123 (2023).
- [49] Stöhr, J. & Siegmann, H. C. Magnetism. *Solid-State Sciences. Springer, Berlin, Heidelberg* **5**, 236 (2006).
- [50] Windsor, Y. W. *et al.* Magnetic properties of strained multiferroic coc r 2 o 4: A soft x-ray study. *Physical Review B* **95**, 224413 (2017).
- [51] Rák, Z., Maria, J.-P. & Brenner, D. Evidence for jahn-teller compression in the (mg, co, ni, cu, zn) o entropy-stabilized oxide: A dft study. *Materials Letters* **217**, 300–303 (2018).
- [52] Acharyya, S. S., Ghosh, S., Adak, S., Sasaki, T. & Bal, R. Facile synthesis of cucr<sub>2</sub>o<sub>4</sub> spinel nanoparticles: a recyclable heterogeneous catalyst for the one pot hydroxylation of benzene. *Catal. Sci. Technol.* **4**, 4232–4241 (2014). URL <http://dx.doi.org/10.1039/C4CY00615A>.
- [53] Galivarapu, J. K. *et al.* Effect of size reduction on cation distribution and magnetic transitions in cocr<sub>2</sub>o<sub>4</sub> multiferroic: Exafs, magnetic and diffused neutron scattering measurements. *RSC Adv.* **6**, 63809–63819 (2016). URL <http://dx.doi.org/10.1039/C6RA10189E>.
- [54] Kaplan, T. & Menyuk, N. Spin ordering in three-dimensional crystals with strong competing exchange interactions. *Philosophical Magazine* **87**, 3711–3785 (2007).
- [55] Kaplan, T. A. Classical theory of spin configurations in the cubic spinel. *Phys. Rev.* **119**, 1460–1470 (1960). URL <https://link.aps.org/doi/10.1103/PhysRev.119.1460>.
- [56] Winkler, E. *et al.* Magnetocrystalline interactions in mn<sub>2</sub>o<sub>4</sub> spinel. *Physical Review B* **80**, 104418 (2009).
- [57] Ederer, C. & Komelj, M. Magnetic coupling in Cocr<sub>2</sub>O<sub>4</sub> and Mn<sub>2</sub>O<sub>4</sub>: An LSDA + U study. *Phys. Rev. B* **76**, 064409 (2007). URL <https://link.aps.org/doi/10.1103/PhysRevB.76.064409>.
- [58] Witte, R. *et al.* High-entropy oxides: An emerging prospect for magnetic rare-earth transition metal perovskites. *Phys. Rev. Mater.* **3**, 034406 (2019). URL <https://link.aps.org/doi/10.1103/PhysRevMaterials.3.034406>.
- [59] Sharma, Y. *et al.* Magnetic anisotropy in single-crystal high-entropy perovskite oxide La(Cr<sub>0.2</sub>Mn<sub>0.2</sub>Fe<sub>0.2</sub>Co<sub>0.2</sub>Ni<sub>0.2</sub>)o<sub>3</sub> films. *Phys. Rev. Mater.* **4**, 014404 (2020). URL <https://link.aps.org/doi/10.1103/PhysRevMaterials.4.014404>.

- [60] Mazza, A. R. *et al.* Charge doping effects on magnetic properties of single-crystal  $\text{La}_{1-x}\text{Sr}_x(\text{Cr}_{0.2}\text{Mn}_{0.2}\text{Fe}_{0.2}\text{Co}_{0.2}\text{Ni}_{0.2})\text{O}_3$  ( $0 \leq x \leq 0.5$ ) high-entropy perovskite oxides. *Phys. Rev. B* **104**, 094204 (2021). URL <https://link.aps.org/doi/10.1103/PhysRevB.104.094204>.
- [61] Mazza, A. R. *et al.* Designing magnetism in high entropy oxides. *Advanced Science* **9**, 2200391 (2022).
- [62] Su, L. *et al.* Direct observation of elemental fluctuation and oxygen octahedral distortion-dependent charge distribution in high entropy oxides. *Nature communications* **13**, 2358 (2022).
- [63] Mugiraneza, S. & Hallas, A. M. Tutorial: a beginner’s guide to interpreting magnetic susceptibility data with the Curie-Weiss law. *Communications Physics* **5**, 95 (2022).
- [64] Coey, J. M. D. *Magnetism And Magnetic Materials* (Cambridge University Press, U.K., 2010).
- [65] Kassem, M. A., El-Fadl, A. A., Nashaat, A. M. & Nakamura, H. Structural, optical and single-domain magnetic features of the noncollinear ferrimagnetic nano-spinel chromites  $\text{ACr}_{1-x}\text{A}_x\text{O}_4$  (A= Ni, Co, and Mn). *arXiv preprint arXiv:2305.17856* (2023).
- [66] Lee, S.-H., Broholm, C., Kim, T., W Ratcliff, I. & Cheong, S.-W. Local spin resonance and spin-Peierls-like phase transition in a geometrically frustrated antiferromagnet. *Physical Review Letters* **84**, 3718 (2000).
- [67] J. Rodríguez-Carvajal. Recent developments of the program fullprof, in commission on powder diffraction (IUCR). *Newsletter* **26**, 12–19 (2001).
- [68] Ravel, B. & Newville, M. Athena, Artemis, Hephaestus: data analysis for X-ray absorption spectroscopy using IFFFIT. *Journal of synchrotron radiation* **12**, 537–541 (2005).
- [69] Kresse, G. & Joubert, D. From ultrasoft pseudopotentials to the projector augmented-wave method. *Phys. Rev. B* **59**, 1758–1775 (1999). URL <https://link.aps.org/doi/10.1103/PhysRevB.59.1758>.
- [70] Kresse, G. & Furthmüller, J. Efficient iterative schemes for ab initio total-energy calculations using a plane-wave basis set. *Phys. Rev. B* **54**, 11169–11186 (1996). URL <https://link.aps.org/doi/10.1103/PhysRevB.54.11169>.
- [71] Perdew, J. P., Burke, K. & Ernzerhof, M. Generalized gradient approximation made simple. *Phys. Rev. Lett.* **77**, 3865–3868 (1996). URL <https://link.aps.org/doi/10.1103/PhysRevLett.77.3865>.



- [72] Dudarev, S. L., Botton, G. A., Savrasov, S. Y., Humphreys, C. J. & Sutton, A. P. Electron-energy-loss spectra and the structural stability of nickel oxide: An lsdau study. *Phys. Rev. B* **57**, 1505–1509 (1998). URL <https://link.aps.org/doi/10.1103/PhysRevB.57.1505>.
- [73] Das, D. & Ghosh, S. Density functional theory based comparative study of electronic structures and magnetic properties of spinel  $\text{acr}_2\text{o}_4$  ( $a = \text{mn, fe, co, ni}$ ) compounds. *Journal of Physics D: Applied Physics* **48**, 425001 (2015). URL <https://dx.doi.org/10.1088/0022-3727/48/42/425001>.
- [74] Wang, L., Maxisch, T. & Ceder, G. Oxidation energies of transition metal oxides within the GGA + U framework. *Phys. Rev. B* **73**, 195107 (2006). URL <https://link.aps.org/doi/10.1103/PhysRevB.73.195107>.
- [75] Himmetoglu, B., Wentzcovitch, R. M. & Cococcioni, M. First-principles study of electronic and structural properties of  $\text{cuo}$ . *Phys. Rev. B* **84**, 115108 (2011). URL <https://link.aps.org/doi/10.1103/PhysRevB.84.115108>.
- [76] Harun, K., Salleh, N. A., Deghfel, B., Yaakob, M. K. & Mohamad, A. A. Dft + u calculations for electronic, structural, and optical properties of  $\text{zno}$  wurtzite structure: A review. *Results in Physics* **16**, 102829 (2020). URL <https://www.sciencedirect.com/science/article/pii/S2211379719327287>.

## ACKNOWLEDGEMENTS

The authors acknowledge the uses of central facilities of the department of Physics, IISc Bangalore, funded by the FIST program of DST (Department of Science and Technology), India. SM acknowledges funding support from a SERB Core Research grant (Grant No. CRG/2022/001906). RN thanks the Indian Institute of Science for support through Sir C. V. Raman postdoctoral fellowship program and Prof. K.R.S. Priolkar for commenting on the manuscript. SD and NB acknowledge funding from the Prime Minister's Research Fellowship (PMRF), MoE, Government of India. UGC-DAE Consortium for Scientific Research, Kalpakkam Node, Kokilamedu is acknowledged for providing SQUID-VSM MPMS facility for conducting magnetic measurements, which is part of this work. Portions of this research were carried out at the light source PETRA III DESY, a member of the Helmholtz Association (HGF). Financial support by the Department of Science & Technology (Government of India) provided within the framework of the India@DESY

collaboration is gratefully acknowledged. This research used resources of the Advanced Photon Source, a U.S. Department of Energy Office of Science User Facility operated by Argonne National Laboratory under Contract No. DE-AC02-06CH11357. This research used resources of the Advanced Light Source, which is a Department of Energy Office of Science User Facility under Contract No. DE-AC02-05CH11231. B.S. acknowledges financial support from Swedish Research Council (grant no. 2022-04309) and STINT Mobility Grant for Internationalization (grant no. MG2022-9386). The computations were enabled by resources provided by the National Academic Infrastructure for Supercomputing in Sweden (NAISS) at UPPMAX (NAISS 2024/5-258) and at NSC and PDC (NAISS 2023/3-42) partially funded by the Swedish Research Council through grant agreement no. 2022-06725. B.S. also acknowledges the allocation of supercomputing hours granted by the EuroHPC JU Development Access call in LUMI-C supercomputer (grant no. EHPC-DEV-2024D04-071) in Finland. S.E. acknowledges the allocation of supercomputing hours granted by the EuroHPC JU Development Access call in LUMI-C supercomputer (grant no. EHPC-DEV-2024D03-043) in Finland and Karolina supercomputer (grant no. EU2023D11-039) in Czech Republic.

#### **AUTHOR CONTRIBUTION**

SM conceived and supervised the project. RN and SD synthesized, characterized the samples and analyzed all results. RN, SD, NB, CK carried out soft X-ray absorption spectroscopy measurements. RN, NB, TD, GES performed EXAFS experiments. S.E. has performed all the calculations based on DFT, and B.S. has supervised the theoretical part. RN and SM wrote the manuscript. All authors discussed the results and commented on the manuscript.

#### **COMPETING INTERESTS**

The authors declare no competing interests.